4. D. K. Lilly, *Q. J. R. Meteorol. Soc.* **94**, 292 (1968).
5. S. Twomey, *Atmos. Environ.* **8**, 1251 (1974).
6. B. A. Albrecht, *Science* **245**, 1227 (1989).
7. J. H. Conover, *J. Atmos. Sci.* **23**, 778 (1966); J. A. Coakley, Jr., R. L. Bernstein, P. A. Durkee, *Science* **237**, 1020 (1987); L. F. Radke, J. A. Coakley Jr., M. D. King, *ibid.* **246**, 1146 (1989); M. D. King, L. F. Radke, P. V. Hobbs, *J. Geophys. Res.* **98**, 2729 (1993).
8. E. E. Hindman, W. M. Porch, J. G. Hudson, P. A. Durkee, in *Proceedings of the 11th International Conference on Clouds and Precipitation*, Montreal, Canada, 17 to 21 August 1992 (Department of Meteorology, McGill University, Montreal, Canada), pp. 184–187.
9. The cloud microphysical model [O. B. Toon, R. P. Turco, D. Westphal, R. Malone, M. S. Liu, *J. Atmos. Sci.* **45**, 2123 (1988)] resolves the distributions of both unactivated CCN and cloud droplets and explicitly treats the warm cloud microphysical processes that affect them. Vertical transport is represented with a turbulent kinetic energy closure scheme [P. G. Duynkerke and A. G. M. Driedonks, *ibid.* **44**, 43 (1987)]. The model uses the radiative transfer scheme of O. B. Toon, C. P. McKay, T. P. Ackerman, and K. Santhanam [*J. Geophys. Res.* **94**, 16287 (1989)].
10. Similar values were estimated by others to be an average CCN production rate [M. B. Baker and R. J. Charlson, *Nature* **345**, 142 (1990); D. A. Hegg, *Geophys. Res. Lett.* **17**, 2165 (1990)]. The distribution of CCN is specified as log-normal with a (number) mean radius of 0.1 μm and a geometric SD of 1.2, similar to surface measurements from the remote, cloud-free Pacific Ocean [A. D. Clarke, N. C. Ahlquist, D. S. Covert, *J. Geophys. Res.* **92**, 4179 (1987)]. Another potential source of CCN, due to subsidence of air from above the boundary layer, was included in sensitivity tests. The constant CCN production rate does not include the possibility that CCN production is favored when particle concentrations are low [X. Lin, W. L. Chameides, C. S. Kiang, A. W. Stelson, H. Berresheim, *J. Geophys. Res.* **97**, 18161 (1992)].
11. The initial temperature profile was adiabatic up to 750 m, where there were jumps in temperature (+6 K) and water vapor (−2 g kg^{-1}). The sea-surface temperature was fixed at 288 K. The downwelling infrared flux at the top of the model (at a height of 1 km) was fixed at 270 W m^{-2}, and the wind speed in the top layer of the model was fixed at the geostrophic value of 5 m s^{-1}. The divergence rate of horizontal wind velocity was constant at 5×10^{-6} s^{-1}.
12. S. Nicholls, *Q. J. R. Meteorol. Soc.* **110**, 783 (1984).
13. S. Nicholls and J. Leighton, *ibid.* **112**, 431 (1986).
14. Solar heating offsets infrared cooling and stabilizes the temperature profile between the cloud and subcloud layers, leading to a decoupling in vertical mixing between the layers (*12*).
15. In Eq. 1 it is assumed that the cloud droplet size distribution is vertically uniform [J. E. Hansen and L. D. Travis, *Space Sci. Rev.* **16**, 527 (1974)]. However, the modeled cloud droplet size distributions varied with height in the cloud. Therefore, we determined an optically representative value of r_{eff} by evaluating it at an altitude corresponding to an optical depth of 1 below cloud top. At time 0 in the second scenario this optically representative altitude occurred 50 m below cloud top; after 2 days this altitude descended to 100 m below cloud top. Values of τ given in Table 1 are calculated from Eq. 1 and are within ~10% of the optical depth calculated by the integration of extinction coefficients over the profile of droplet size distributions (Fig. 2D). Cloud thickness is taken to be the difference between the altitudes at which visibility is <1 km. The average liquid-water content is calculated by dividing the vertically integrated liquid-water path by *h*.
16. For this comparison, calculations of the albedo at the top of the atmosphere were made at a constant solar zenith angle of 60°. The cloud-free albedo in the model was 12%.
17. In the diurnal average of scenario 2 before time 0, there are differences between the above-cloud values and the cloud-top values of +2 K in equivalent potential temperature and −2 g kg^{-1} in the total water mixing ratio. Therefore, cloud-top entrainment instability could not have occurred in our simulations [D. A. Randall, *J. Atmos. Sci.* **37**, 125 (1980); H. Kuo and W. H. Schubert, *Q. J. R. Meteorol. Soc.* **114**, 887 (1988); M. K. MacVean and P. J. Mason, *J. Atmos. Sci.* **47**, 1012 (1990)].
18. Solar heating has been suggested as a precursor to the breakup of marine stratiform clouds by D. P. Rogers and D. Koracin [*J. Atmos. Sci.* **49**, 1473 (1992)]. Although the cloud dissipation shown in Fig. 2 occurred near sunrise, this was coincidental. A variation on our second scenario in which the reduction to the lower CCN production rate was delayed 12 hours led to a collapse of the boundary layer that was also delayed by 12 hours.
19. Averaged over the depth of the boundary layer, the particle source due to subsidence is the product of the divergence rate and the concentration of CCN above the boundary layer. A divergence of 3×10^{-6} s^{-1} and a CCN concentration of 100 cm^{-3} provide 3×10^{-4} particles per cm^3 per s to the boundary layer.
20. S. Twomey, H. B. Howell, T. A. Wojciechowski, *J. Atmos. Sci.* **25**, 333 (1968); D. A. Hegg, R. J. Ferek, P. V. Hobbs, L. F. Radke, *J. Geophys. Res.* **96**, 13189 (1991); D. A. Hegg, L. F. Radke, P. V. Hobbs, *ibid.*, p. 18727.
21. C. J. Bowley, *J. Atmos. Sci.* **24**, 596 (1967).
22. A strong injection of CCN under these conditions would cause an increase in droplet concentrations. This would lead to a reduction in droplet sizes, which would cause a decrease in drizzle, allowing an increase in cloud liquid water. The ultimate result, the triggering of a visible ship track, would be an enhancement of cloud optical depth substantial enough to drive vertical mixing through cloud-top radiative cooling.
23. This work was supported by the National Aeronautics and Space Administration (NASA), the U.S. Department of Energy, and the National Science Foundation. Computations were performed at the Numerical Aerodynamic Simulation Program facility at NASA Ames Research Center.

20 April 1993; accepted 20 August 1993

High-Temperature XAS Study of Fe_2SiO_4 Liquid: Reduced Coordination of Ferrous Iron

W. E. Jackson,* J. Mustre de Leon, G. E. Brown Jr.,† G. A. Waychunas, S. D. Conradson, J.-M. Combes

X-ray absorption spectroscopy (XAS) of Fe^{2+} in Fe_2SiO_4 liquid at 1575 kelvin and 10^{-4} gigapascal (1 bar) shows that the Fe^{2+}–O bond length is 1.98 ± 0.02 angstroms compared with ≈2.22 angstroms in crystalline Fe_2SiO_4 (fayalite) at the melting point (1478 kelvin), which indicates a decrease in average Fe^{2+} coordination number from six in fayalite to four in the liquid. Anharmonicity in the liquid was accounted for using a data analysis procedure. This reduction in coordination number is similar to that observed on the melting of certain ionic salts. These results are used to develop a model of the medium-range structural environment of Fe^{2+} in olivine-composition melts, which helps explain some of the properties of Fe_2SiO_4 liquid, including density, viscosity, and the partitioning of iron and nickel between silicate melts and crystalline olivines. Some of the implications of this model for silicate melts in the Earth's crust and mantle are discussed.

Ferrous iron (Fe^{2+}) is the major transition metal in mafic and ultramafic silicate melts in the Earth's lower crust and upper mantle (*1*) and in some metallurgical slags. In such liquids, Fe^{2+} is commonly believed to be six-coordinated by oxygens (*2*), but it might be four- or five-coordinated as well (*3*, *4*). Such differences in iron coordination would have a significant effect on the physical properties of these liquids, particularly on their density, viscosity, and ionic diffusivity, because of expected increases in metal-oxygen bond strength with decreasing coordination number and bond length. Thus, knowledge of the local coordination environment of Fe^{2+} in silicate liquids as a function of temperature is necessary to understand these and other properties and to help constrain models of Earth's partially molten interior (*5*).

There is little direct information about the coordination environments of transition metals in silicate liquids because structural studies of liquids at temperatures >1000 K are experimentally difficult and techniques such as nuclear magnetic resonance (NMR) and Raman spectroscopy, which have provided valuable information on the polymeric structure of silicate liquids, are not well suited for studies of transition-metal environments. Most information on the effects of temperature, pressure, and composition on the structure of such melts, including the coordination environment of transition metals, has been derived by inference and extrapolation from

W. E. Jackson and G. E. Brown Jr., Department of Geological and Environmental Sciences and Stanford Synchrotron Radiation Laboratory, Stanford University, Stanford, CA 94305.
J. Mustre de Leon and S. D. Conradson, Electronics Research Group, Los Alamos National Laboratory, Los Alamos, NM 87545.
G. A. Waychunas, Center for Materials Research, Stanford University, Stanford, CA 94305.
J.-M. Combes, St. Gobain Inc. Recherche, 93304 Aubervilliers, France.

*Present address: General Electric Company, 6325 Huntley Road, Post Office Box 568, Worthington, OH 43085.
†To whom correspondence should be addressed.

structural studies of silicate glasses under ambient conditions (*2*), from studies of silicate phase equilibria (6), and from silicate crystal-liquid partitioning behavior of selected elements (*7*).

Two studies that provided direct information on the local environment of Fe^{2+} in silicate melts at high temperature are an x-ray scattering investigation of melts from the FeO-SiO_2 binary system (8) and an iron extended x-ray absorption fine structure (EXAFS) spectroscopy study of melts of composition $M_2FeSi_3O_8$ (M = Li, Na, K) (*4*). The x-ray scattering study suggested that Fe^{2+} is bonded to six nearest neighbor oxygens in FeO-rich liquids but that it loses two oxygens from its first coordination shell in more SiO_2-rich liquids, including molten Fe_2SiO_4 (8). However, the radial distribution function (RDF) derived for Fe_2SiO_4 liquid yielded an unrealistic Fe–O–Si bond angle of 55°, which casts some doubt on these results. The XAS technique provides element-specific structural information and thus helps overcome some of the difficulties encountered in x-ray scattering studies. However, interatomic distances derived from high-temperature XAS are sensitive to anharmonic effects, which must be taken into account in XAS data analysis (9). The high-temperature Fe-XAS investigation (*4*) showed that Fe^{2+} is dominantly four-coordinated in $M_2FeSi_3O_8$ melts.

In this report we describe XAS measurements of the Fe^{2+} coordination environment in Fe_2SiO_4 melt at 1575 K and 10^{-4} GPa. Although this melt is structurally and compositionally simpler than natural ultramafic magmas in Earth's lower crust and upper mantle, the model we develop for the medium-range environment (<5 Å) around Fe^{2+} in Fe_2SiO_4 liquid has implications for structure-property relations in natural ultramafic magmas.

We collected high-temperature Fe K-edge XAS data at the National Synchrotron Light Source (Brookhaven National Laboratory) on beam line X19A in the fluorescence mode using Si(111) monochromator crystals and a controlled-atmosphere furnace (*10*) that contained the liquid sample resting on a BeO surface (*11*). The starting composition was synthetic fayalite (*12*). X-ray diffraction and ^{57}Fe Mössbauer data collected from the recrystallized sample, after melting, are consistent with fayalite and show that >96% of the iron is Fe^{2+}. The small amount of Fe^{3+} present may have resulted from incongruent melting of fayalite (*12*), and it had no significant effect on our XAS results.

A single-crystal x-ray diffraction study of fayalite as a function of temperature (*13*) showed that Fe^{2+} remains octahedrally coordinated by oxygens to at least 1198 K and that the mean Fe^{2+}–O bond expands positively and continuously from 2.168 ± 0.004 Å at 298 K to 2.195 ± 0.009 Å at 1198 K. The relative enthalpies ($H_T - H_{300}$) of crystalline and molten Fe_2SiO_4 measured over the temperature range 985 to 1705 K (*14*) increase smoothly up to the melting point, suggesting that fayalite does not undergo major structural rearrangement, including cation coordination changes, before melting. Extrapolation of the Fe^{2+}–O bond length versus temperature trend (*13*) to the melting point yields a predicted value of ≈2.22 Å for the mean $^{VI}Fe^{2+}$–O bond length in fayalite at the melting point (1478 K).

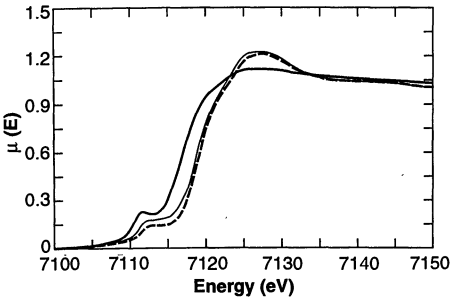

Fig. 1. Fe K-XANES data for the Fe_2SiO_4 crystal before melting at 298 K (dashed line), in the liquid state at 1575 K (heavy solid line), and at 298 K after recrystallization (light solid line). The slight (<1 eV) shift in the main edge position provides additional support for the observation that Fe^{2+} did not oxidize in the melt. The intensity of the $1s \rightarrow 3d$ transition of recrystallized fayalite is slightly greater than the same feature in the fayalite XANES spectrum before melting. This difference may be due to the presence of some of the Fe^{3+} cations (<4% of total iron) in noncentrosymmetric sites of recrystallized fayalite. Iron metal was used as an energy calibration standard.

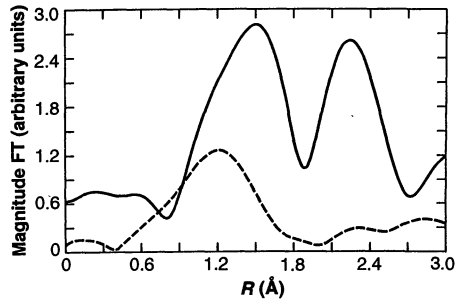

Fig. 2. Fe K-EXAFS Fourier transformed (FT) data for Fe_2SiO_4 liquid at 1575 K (dashed line), uncorrected for phase shift and anharmonicity, and for fayalite at 298 K (solid line), uncorrected for phase shift. Note the large decrease in *R* from the crystal spectrum to the liquid spectrum.

The Fe K-edge x-ray absorption near-edge structure (XANES) of fayalite, the high-temperature liquid, and recrystallized fayalite (after melting) are shown in Fig. 1. The XANES spectrum of the liquid exhibits a $1s \rightarrow 3d$ transition feature at 7112 eV that is about twice as intense as that for the crystal, both before and after melting, which strongly supports $^{IV}Fe^{2+}$ in the liquid (*15, 16*). Fourier transforms of the EXAFS data for Fe_2SiO_4 liquid (1575 K) and fayalite (298 K) (Fig. 2) suggest that the average Fe^{2+}–O distance in the liquid is substantially less than that in the crystal at 298 K and 10^{-4} GPa (*17*). The high-temperature liquid data, however, have not been corrected for anharmonic effects, which are known to cause erroneously short first-neighbor bond distances when derived by conventional (harmonic) EXAFS modeling procedures (*9, 18*). To provide an accurate measure of the average Fe–O distance in the liquid, $\mathbf{R}_{liq}$, we evaluated the anharmonic and static contributions to the phase of the EXAFS signal from Fe–O polyhedra in the liquid using two models as described below.

In both models, the total observed Fe K-EXAFS phase for Fe_2SiO_4 liquid is given by

$$\Phi_{(k)_{liq}} = 2\mathbf{kR}_{liq} + \phi(k)_{sc} + \phi(k)_{anh} \quad (1)$$

where $\phi(k)_{sc}$ is the phase-shift due to the back-scattering (oxygen) and absorbing (iron) atoms, $\phi(k)_{anh}$ is the anharmonic contribution to the observed phase at 1575 K, $\mathbf{R}_{liq}$ is the Fe^{2+}–O bond distance in the liquid, and **k** denotes the photoelectron wave vector {$= [0.2625(E - E_0)]^{1/2}$}. In the first model we assumed that the local environments of Fe^{2+} in the liquid and high-temperature crystal are similar (Fe^{2+} is six-coordinated by oxygen and the average $^{VI}Fe^{2+}$–O distance is ≈2.22 Å), which implies that the harmonic portion of the Fe-O potential in the high-temperature crystal and in the liquid are similar. The total EXAFS phase of fayalite at 298 K, where anharmonic effects can be neglected, is given by

$$\Phi_{(k)_{xtl}} = 2\mathbf{kR}_{xtl} + \phi(k)_{sc} \quad (2)$$

where $\mathbf{R}_{xtl}$ is the average Fe–O distance in the crystal. From Eqs. 1 and 2 we obtain

$$\mathbf{R}_{liq} = \mathbf{R}_{xtl} + \langle[\Phi_{(k)_{liq}} - \Phi_{(k)_{xtl}}]/2\mathbf{k}\rangle - \langle\phi(k)_{anh}/2\mathbf{k}\rangle \quad (3)$$

where $\langle f \rangle$ denotes the average function $f(k)$ over the **k** range of interest ($\Delta\mathbf{k} = \mathbf{k}_2 - \mathbf{k}_1$) and is defined as

$$\langle f \rangle = \frac{1}{\Delta k}\int_{k_1}^{k_2} f(k)dk \quad (4)$$

To evaluate Eq. 3, we first determined the function $[\Phi_{(k)_{liq}} - \Phi_{(k)_{xtl}}]/2\mathbf{k}$ for Fe_2SiO_4 by subtracting the EXAFS phase functions extracted from the Fourier transforms shown in Fig. 2. Upon integrating this function

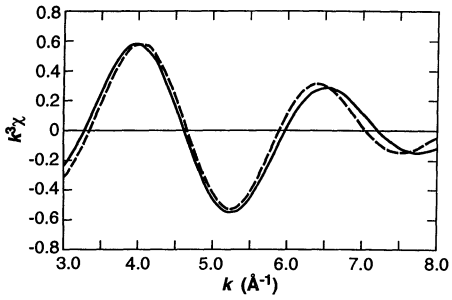

Fig. 3. Harmonic fit (dashed line) to the $k^3\chi(k)$ function for Fe_2SiO_4 liquid Fe K-EXAFS data (solid line). This fit gave $\mathbf{R}_{app}$ = 1.88 ± 0.01 Å. With $<\phi(k)_{anh}/2\mathbf{k}>$ = 0.10 ± 0.01 Å, the true Fe^{2+}–O bond distance in Fe_2SiO_4 liquid, $\mathbf{R}_{liq}$, is 1.98 ± 0.02 Å.

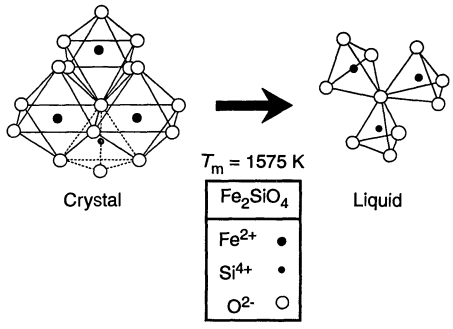

Fig. 4. Model for the structural change around an average oxygen in the Fe_2SiO_4 crystal-to-melt transition. This model is charge-balanced and consistent with the stoichiometry and Pauling's bond strength rule (see text), where bond strength is defined as cation charge divided by cation coordination number.

over the **k** range of 3 to 9 Å^{-1}, we obtained a value of −0.22 Å. Next, we evaluated the temperature-dependent anharmonic motion of oxygen in the Fe–O bond of Fe_2SiO_4 liquid by assuming that the Fe-O anharmonicity is the same in the liquid as in two well-characterized crystalline reference compounds at the same temperature. To accomplish this, we fit asymmetric potential functions to Fe K-EXAFS data over a range of temperatures (90 to ≈1200 K) from $(Mg_{0.9}Fe_{0.1})O$ (magnesiowüstite) and $Ca_3Fe_2Si_3O_{12}$ (andradite), both of which have well-known Fe–O bond length expansions with increasing temperature (*19*). Each of these compounds contains iron in six-coordinated, centrosymmetric sites with little static disorder. The value of $\langle\phi(k)_{anh}/2\mathbf{k}\rangle$ at 1575 K is −0.10 ± 0.01 Å (*18*). Knowing that $\mathbf{R}_{xtl}$ for fayalite at 298 K is 2.168 ± 0.004 Å (*13*), $\mathbf{R}_{liq}$ is 2.05 ± 0.02 Å from Eq. 3. This distance is substantially less than that predicted (2.22 Å) for fayalite at 1575 K and leads to a predicted bond length change of −0.12 Å in fayalite over the temperature range 298 to 1575 K. This prediction is not consistent with the observed Fe–O bond-length expansion of fayalite over the same temperature range (+0.05 Å), and thus our assumption that the average, local environment of Fe^{2+} in the liquid is the same as that in fayalite at the melting temperature is not correct.

In the second model we did not assume that the Fe^{2+} environments, and hence the Fe-O potentials, of the liquid and crystal are similar. Instead, we carried out a harmonic analysis of the Fe_2SiO_4 liquid EXAFS data that models the Gaussian portion of the RDF of Fe^{2+} in a fashion analogous to that for the low-temperature crystal EXAFS data. We modeled the non-Gaussian portion of the RDF using the anharmonic analysis described above. The total phase of the liquid is expressed as

$$\Phi_{(k)_{liq}} = 2\mathbf{k}\mathbf{R}_{app} + \phi(k)_{sc} \quad (5)$$

where $\mathbf{R}_{app}$ is the apparent Fe^{2+}–O distance in the liquid assuming only harmonic motion for oxygen (Fig. 3). This fitting process yields $\mathbf{R}_{app}$ = 1.88 ± 0.01 Å, a value that is unrealistically short because the anharmonic contributions to the phase are neglected. We can correct $\mathbf{R}_{app}$ for anharmonicity by combining Eqs. 1 and 5 to give

$$\mathbf{R}_{liq} = \mathbf{R}_{app} - <\phi(k)_{anh}/2\mathbf{k}> \quad (6)$$

where $\langle\phi(k)_{anh}/2\mathbf{k}\rangle$ = −0.10 ± 0.01 Å. Therefore, we conclude that the average Fe^{2+}–O bond length, $\mathbf{R}_{liq}$, in Fe_2SiO_4 liquid at 1575 K and 10^{-4} GPa is 1.98 ± 0.02 Å.

This bond distance is similar to that of tetrahedrally coordinated Fe^{2+} in crystalline silicates and oxides at 298 K and 10^{-4} GPa, which ranges from 1.96 to 2.01 Å, and is significantly smaller than the Fe–O distance for octahedral Fe^{2+} in these materials, which ranges from 2.08 to 2.18 Å (*4*, *16*). If static disorder (estimated from the range of bond distances) in the first-neighbor coordination environment of Fe^{2+} in Fe_2SiO_4 liquid were as large as that in crystalline fayalite at 298 K (σ_{static} ≈ 0.17 Å) (*13*), $\mathbf{R}_{app}$ and $\mathbf{R}_{liq}$ should be within +0.03 Å of the values reported above, based on fits of the Fe K-EXAFS data for crystalline fayalite at 298 K (*20*). Neglect of possible differences in static disorder between fayalite and Fe_2SiO_4 liquid should be offset by overestimation of $\langle\phi(k)_{anh}/2\mathbf{k}\rangle$ associated with the reduction in coordination number of Fe^{2+} because the shorter, stronger ^{IV}Fe–O bonds in the liquid should be less anharmonic than ^{VI}Fe–O bonds in the reference compounds at the same temperature. Moderate asymmetry in the liquid Fe-O pair distribution function that arises from static disorder effects will be included in the asymmetry in the pair distribution function due to thermal effects (9).

Our study thus indicates that Fe^{2+} coordination changes from octahedral in fayalite to tetrahedral, on average, in Fe_2SiO_4 melt with an average Fe–O distance of 1.98 ± 0.02 Å. A similar decrease in the coordination number of Al^{3+} was observed with the use of ^{27}Al NMR spectroscopy when α-Al_2O_3 was melted (*21*). In addition, high-temperature scattering studies of some molten salts derived from B1 salt structures have found contractions of up to 0.3 Å of the M^+-Cl^- bond (M = Na, K, Rb) and a decrease in the M^+ coordination number from six to approximately four across the fusion temperature (*22*). These experimental observations, in combination with conclusions from other structural studies of silicate glasses and liquids (*23*), suggest that the coordination numbers of cations like aluminum, magnesium, and Fe^{2+} may decrease in oxide or silicate crystal-to-melt transitions at or near ambient pressures. However, caution must be used in extrapolating structural information derived from glasses under ambient conditions to melts of the same composition at high temperatures (*24*).

A plausible model for the local structure around Fe^{2+} in Fe_2SiO_4 liquid is one in which Fe^{2+} and Si^{4+} are tetrahedrally coordinated and oxygen is coordinated by two $^{IV}Fe^{2+}$ and one $^{IV}Si^{4+}$ (Fig. 4). This arrangement is similar to that in the Zn_2SiO_4 (willemite) structure (*25*), but it is different from that in fayalite, which is hexagonal closest packed with iron in octahedral coordination (*26*) (Fig. 4). In contrast, the Zn_2SiO_4 structure is not closest packed and has relatively large-diameter channels (≈2 Å) parallel to the *c* axis (*25*). This structural model and the shift of Fe^{2+} cations from octahedral sites in fayalite to tetrahedral sites in Fe_2SiO_4 melt accounts for the positive volume change observed on melting fayalite at low pressure (change in volume on melting ≈ +11%) (*27*) and the anomalous thermal expansivity of Fe_2SiO_4 liquid relative to other liquids from the FeO-SiO_2 binary system (*27*). Calculation of Fe_2SiO_4 liquid density at 1575 K, for a willemite-like structure model, yields a value of 3.86 g cm^{-3} (*28*), which is close to the experimental value of 3.75 g cm^{-3} at 1575 K (*27*). A similar calculation, if we assume that the liquid has an average structure like that of fayalite at 1575 K, yields a density of 4.24 g cm^{-3}.

Shiraishi *et al.* found that the viscosity of liquids along the FeO-SiO_2 join increases from FeO to SiO_2 with a local maximum at the Fe_2SiO_4 composition, which they attributed to the presence of regions having fayalite-like structure (that is, $^{VI}Fe^{2+}$) (*27*). This hypothesis is not supported by our results. We suggest instead that the presence of Fe_2SiO_{10} units (Fig. 4) with strong, short Fe–O bonds in Fe_2SiO_4 liquid should result in greater viscosity relative to liquids with lower SiO_2 contents because such liquids have dominantly $^{VI}Fe^{2+}$ (*8*) and

thus weaker Fe–O bonds. For liquid compositions more silica-rich than Fe_2SiO_4, the melt structure must rearrange locally, as indicated by the small local decrease and then rapid increase in viscosity. X-ray scattering studies of FeO-SiO_2 liquids with 39 and 44 mole % SiO_2 are consistent with dominantly $^{IV}Fe^{2+}$ (*8*), and EXAFS studies of even more silica-rich liquids ($M_2FeSi_3O_8$) also find dominantly $^{IV}Fe^{2+}$ (*4*, *29*). Thus the first-neighbor environment of Fe^{2+} appears to remain constant in liquids more silica-rich than Fe_2SiO_4 in this system and is not an important factor in determining their viscosity. In contrast, variations in the medium-range (<5 Å) structure around Fe^{2+} in concert with changes in SiO_4 polymerization must play a key role in the decrease in viscosity of liquids with 33 to 39 mole % SiO_2.

The presence of dominantly $^{IV}Fe^{2+}$ in Fe_2SiO_4 liquid has implications for partitioning of first-row transition elements between coexisting olivine crystals and silicate melts (*7*, *30*). In olivine-composition liquids Fe^{2+} has been assumed to occupy octahedral sites (*2*, *31*) in contrast to our results. A similar assumption is commonly made for Ni^{2+}. The data of Takahashi (*7*) show the order of preference Ni > Co > Fe > Mn for olivine relative to coexisting $(Mg_{0.5}Fe_{0.5})_2SiO_4$-$K_2O{\cdot}4SiO_2$ liquids, which is the order of their octahedral site preference energies (OSPE). These observations suggest that the liquid has fewer octahedral sites than the crystal. Comparison of OSPE for Fe^{2+} (≈0.17 eV) (*32*) with kT (≈0.14 eV at 1575 K) indicates that Fe^{2+} should not show strong preference for octahedral sites in the crystal or liquid at this temperature. Our study shows it is four-coordinated in the liquid. For Ni^{2+} OSPE is much larger (≈0.9 eV) (*32*), and thus Ni^{2+} should be stabilized in octahedral sites in the liquid (at 1575 K), if they exist. Although little is known about the local environment of Ni^{2+} in olivine-composition liquids, Ni^{2+} was found to be dominantly tetrahedral and pentahedral in more SiO_2-rich glasses [$CaNiSi_2O_6$ and $(Na,K)_2NiSi_3O_8$] (*33*) and is dominantly tetrahedral in $Na_2Si_2O_5$ liquid (*34*). Thus, the existing high-temperature structural data for Ni^{2+} and Fe^{2+} in silicate liquids do not support the general assumption that these cations are six-coordinated (*2*).

If natural ultramafic melts also contain four-coordinated Fe^{2+}, a pressure-induced coordination change from ^{IV}Fe to ^{VI}Fe in these melts is possible (*4*, *35*), with attendant changes in the density and, therefore, the buoyancy of ultramafic melts in the Earth's low-velocity zone. A recent in situ Raman spectroscopic study of alkali germanate melts at pressures up to 2.2 GPa (*36*) found evidence for this type of coordination change for germanium, which behaves like silicon in silicates. Simultaneous high-temperature, high-pressure EXAFS studies of Fe_2GeO_4 and Ni_2GeO_4 liquids are required to test this hypothesis for Fe^{2+} and Ni^{2+} in compositionally simple liquids.

REFERENCES AND NOTES

1. T. S. Duffy and D. L. Anderson, *J. Geophys. Res.* **94**, 1895 (1989); D. Shimozuru, *J. Phys. Earth* **11**, 19 (1963); D. L. Anderson and C. Sammis, *Phys. Earth Planet. Inter.* **3**, 41 (1970).
2. J. A. Boon and W. S. Fyfe, *Chem. Geol.* **10**, 287 (1972); D. S. Goldman and J. I. Berg, *J. Non-Crystal. Solids* **38-39**, 183 (1980); G. Calas and J. Petiau, *Bull. Minéral.* **106**, 33 (1983); B. O. Mysen, *Structure and Properties of Silicate Melts* (Elsevier, New York, 1988), pp. 147–186; H. Keppler, *Am. Mineral.* **77**, 62 (1992).
3. F. A. Cotton and G. Wilkinson, *Advanced Inorganic Chemistry* (Wiley-Interscience, New York, ed. 5, 1988), pp. 711–723.
4. G. A. Waychunas, G. E. Brown Jr., C. W. Ponader, W. E. Jackson, *Nature* **332**, 251 (1988).
5. E. Stolper, D. Walker, B. H. Hager, J. F. Hays, *J. Geophys. Res.* **86**, 6261 (1981); S. M. Rigden, T. J. Ahrens, E. M. Stolper, *Science* **226**, 1071 (1984); C. T. Herzberg, in *Magmatic Processes: Physicochemical Principles*, B. O. Mysen, Ed. (Geochemical Society, University Park, PA, 1987), pp. 47–58; T. J. Shankland, U. Nitsan, A. G. Duba, *J. Geophys. Res.* **84**, 1603 (1979).
6. I. Kushiro, *Am. J. Sci.* **275**, 411 (1975).
7. E. Takahashi, *Geochim. Cosmochim. Acta* **42**, 1829 (1978).
8. Y. Waseda and J. M. Toguri, *Metall. Trans. B* **9**, 595 (1978).
9. P. Eisenberger and G. S. Brown, *Solid State Commun.* **29**, 481 (1979); J. M. Tranquada and R. Ingalls, *Phys. Rev. B* **28**, 3520 (1983).
10. The furnace consisted of molybdenum windings and a molybdenum block, which held the BeO sample holder. Nitrogen gas flowing through the sample housing at a rate of about a liter per minute was found to provide an oxygen fugacity (fO_2) value near that of the Mo/MoO_2 buffer, which prevented oxidation or reduction of Fe^{2+} in fayalite and Fe_2SiO_4 liquid at the temperatures of our experiment.
11. Inductively coupled plasma emission spectroscopy and electron microprobe analysis (using the difference method) indicate that less than 1.5% (by weight) BeO entered the liquid. Examination of fayalite samples after melting by scanning electron microscopy suggests that this small fraction of sample holder material most likely enters the liquid as an immiscible phase.
12. Electron microprobe, x-ray diffraction, x-ray absorption spectroscopy, and Mössbauer spectroscopy were used to confirm this phase, its composition, and the fact that less than 4% of the iron was Fe^{3+}. No evidence was found in the Mössbauer spectrum of the quenched Fe_2SiO_4 (after melting) for an oxide phase.
13. J. R. Smyth, *Am. Mineral.* **60**, 1092 (1975).
14. J. F. Stebbins and I. S. E. Carmichael, *ibid.* **69**, 292 (1984).
15. The $1s \rightarrow 3d$ electronic transition is predicted and observed to be weak when Fe^{2+} is in a centrosymmetric environment, such as an octahedron with O_h symmetry, and is enhanced in noncentrosymmetric environments, with the greatest intensification observed for tetrahedral sites. The observed pre-edge intensity in Fe_2SiO_4 liquid is in good agreement with that found for tetrahedral model compounds. Fayalite, in which Fe^{2+} occupies distorted octahedra, shows the highest observed intensity for a six-coordinated Fe^{2+} site among a number of iron oxide and iron silicate reference compounds (*4*, *16*). Thus, a reduction in Fe^{2+} coordination is the most likely cause of the higher pre-edge intensity of Fe_2SiO_4 liquid relative to fayalite.
16. G. A. Waychunas, G. E. Brown Jr., M. J. Apted, *Phys. Chem. Minerals* **10**, 1 (1983).
17. We were unable to model the amplitude of the liquid Fe K-EXAFS data to derive coordination numbers because of the thermal damping of the EXAFS signal and self-absorption of the fluorescence photons by the sample in this experimental configuration. However, a strong positive correlation exists between the average bond distance in a polyhedron and the number of coordinating ligands [R. D. Shannon, *Acta Crystallogr. Sect. A* **32**, 751 (1976); ——— and C. T. Prewitt, *Acta Crystall. Sect. B* **25**, 925 (1969)].
18. We have analyzed the effects of anharmonic motion of oxygens on high-temperature Fe K-EXAFS data using Fe-O pair potential functions derived from temperature-dependent EXAFS studies of iron-bearing crystalline silicates and oxides for which the thermal expansivity of the Fe–O bond is well known. In each case the anharmonic correction, $\langle\phi(k)_{anh}/2\mathbf{k}\rangle$, to the apparent (harmonic) high-temperature (1575 K) Fe–O distance, $\mathbf{R}_{app}$, was found to be −0.10 ± 0.01 Å [W. E. Jackson *et al.*, in *XAFS VI: X-ray Absorption Fine Structure VI*, S. S. Hasnain, Ed. (Ellis Horwood Ltd., Chichester, UK, 1991), pp. 298–301; J. Mustre de Leon *et al.*, *ibid.*, pp. 54–57.
19. I. Suzuki, *J. Phys. Earth* **23**, 145 (1975); R. J. Rakai, thesis, University of British Columbia (1975).
20. We used a single Gaussian shell of oxygen distances to approximate the slightly asymmetric distribution of oxygens around Fe^{2+} in crystalline fayalite. This fit yielded an Fe–O distance that is 0.02 Å smaller than the Fe–O distance in fayalite (2.168 ± 0.004 Å) determined by single-crystal x-ray diffraction at 298 K (*13*).
21. D. Massiot, F. Taulelle, J. P. Coutures, *Colloq. Phys.* **C5-18**, 425 (1990).
22. S. Biggin and J. E. Enderby, *J. Phys. C* **15**, L305 (1982); N. H. March, R. A. Street, M. Tosi, Eds., *Amorphous Solids and the Liquid State* (Plenum, New York, 1985).
23. Y. Waseda, *The Structure of Non-Crystalline Materials* (McGraw-Hill, New York, 1980); C. D. Yin, M. Okuno, H. Morikawa, F. Marumo, *J. Non-Crystal. Solids* **55**, 131 (1983); Y. Matsui, K. Kayamura, Y. Syono, in *High Pressure Research in Geophysics*, S. Akimoto and M. H. Manghnani, Eds. (Reidel, Dordrecht, Holland, 1982), pp. 511–524.
24. The average Fe^{2+}–O bond length in Fe_2SiO_4 melt (1.98 ± 0.02 Å) is slightly shorter than that (2.02 ± 0.02 Å) found in a room-temperature Fe XAS study of Fe_2SiO_4 glass produced by rapid splat quenching (W. E. Jackson, G. E. Brown Jr., G. A. Waychunas, T. F. Cooney, in preparation). This difference is consistent with the presence of four- and five-coordinated Fe^{2+} in Fe_2SiO_4 glass and dominantly four-coordinated Fe^{2+} in Fe_2SiO_4 melt. The difference may be due to rapid structural rearrangements of the liquid during the quench, because the melting temperature (T_m) is several hundred kelvin higher than the glass-transition temperature (T_g), and the liquid structure may have changed significantly between T_m and T_g [M. E. Brandriss and J. F. Stebbins, *Geochim. Cosmochim. Acta* **52**, 2659 (1988); J. F. Stebbins, *J. Non-Crystal. Solids* **106**, 359 (1988); E. M. Stolper and T. J. Ahrens, *Geophys. Res. Lett.* **14**, 1231 (1987); J. F. Stebbins and I. Farnan, *Science* **255**, 586 (1992)].
25. C. Hang, M. A. Simonov, N. V. Belov, *Soviet Phys.-Crystallogr.* **15**, 387 (1970).
26. G. E. Brown Jr., in *Reviews in Mineralogy*, vol. 5, *Orthosilicates*, P. H. Ribbe, Ed. (Mineralogical Society of America, Washington, DC, ed. 2, 1982), pp. 275–382.
27. Y. Shiraishi, K. Ikeda, A. Tamura, T. Saito, *Trans. Jpn. Inst. Metals* **19**, 264 (1978); R. L. Lange and I. S. E. Carmichael, in *Reviews in Mineralogy*, vol. 24; *Modern Methods of Igneous Petrology: Understanding Magmatic Processes*, J. Nichols and J. K. Russell, Eds. (Mineralogical Society of America, Washington, DC, 1990), pp. 25–64.
28. One can estimate the density of Fe_2SiO_4 liquid at

1575 K using the unit cell volume of Zn_2SiO_4 at 298 K (1577.8 Å^3) and substituting iron for zinc in the formula unit (the number of formula units of Zn_2SiO_4 in the unit cell of the willemite structure is 18). The small difference between the value derived by this method (3.86 g cm^{-3}) and the experimentally determined value (3.75 g cm^{-3}) can be accounted for by increasing Fe–O–Si angles or allowing for the slightly longer Fe–O bond (≈1.98 Å) relative to the Zn–O bond (≈1.958 Å) (*25*) in the model.

29. W. E. Jackson *et al.*, *Eos* **71**, 1665 (1990); in preparation.
30. T. N. Irvine and I. Kushiro, *Carnegie Inst. Washington Yearb.* **75**, 668 (1976); A. J. Irving, *Geochim. Cosmochim. Acta* **42**, 743 (1978).
31. R. G. Burns and W. S. Fyfe, in *Researches in Geochemistry*, vol. 2, P. H. Abelson, Ed. (Wiley, New York, 1967), pp. 259–285.
32. R. G. Burns, *Mineralogical Applications of Crystal Field Theory* (Cambridge Univ. Press, Cambridge, 1970), pp. 109–112.
33. L. Galoisy and G. Calas, *Am. Mineral.* **76**, 1777 (1991); *Geochim. Cosmochim. Acta*, in press.
34. F. Farges, G. E. Brown Jr., G. Calas, L. Galoisy, G. A. Waychunas, in preparation.
35. H. S. Waff, *Geophys. Res. Lett.* **2**, 193 (1975).
36. D. L. Farber and Q. Williams, *Science* **256**, 1427 (1992).
37. We thank S. Bohlen for providing the synthetic fayalite for this study, S. Cramer for assisting in the data collection, and M. Brandriss and E. Winterburn for assisting in the sample characterization. Helpful reviews were provided by J. I. Brauman and J. F. Stebbins and by two anonymous referees. This work was supported by the National Science Foundation (Stanford) and the Department of Energy (Los Alamos).

26 July 1993; accepted 6 August 1993

Teosinte glume architecture 1: A Genetic Locus Controlling a Key Step in Maize Evolution

Jane Dorweiler, Adrian Stec, Jerry Kermicle, John Doebley*

Teosinte, the probable progenitor of maize, has kernels that are encased in hardened fruitcases, which interfere with the use of the kernels as food. Although the components of the fruitcase are present in maize, their development is disrupted so that the kernels are not encased as in teosinte but exposed on the ear. The change from encased to exposed kernels represents a key step in maize evolution. The locus that largely controls this morphological difference between maize and teosinte, *teosinte glume architecture 1*, is described and genetically mapped.

Genetic and biosystematic research has provided substantial evidence that maize is a domesticated derivative of the wild Mexican grass teosinte (*Zea mays* ssp. *parviglumis*) (*1*–*6*). Nevertheless, because of the profound architectural differences between the maize and teosinte ears, the precise morphogenetic steps involved in the transition from teosinte to maize remain in doubt (*7*–*9*). In this report we describe a genetic locus, *teosinte glume architecture 1* (*tga1*), that controls a key difference in ear development between teosinte and maize: It alters the development of the teosinte cupulate fruitcase so that the kernel is exposed on the ear for easy harvest. The existence of this locus supports the view (*1*, *7*) that a small number of single-gene changes could account for the transformation of teosinte into maize.

The cupulate fruitcase of teosinte is composed of a rachis internode (or rachid) and the attached spikelet (Fig. 1). In the teosinte ear, the rachids are deeply invaginated such that the mature spikelet (including the kernel) fits within this invagination, or cupule. The spikelet is composed of a female flower and a series of bracts that subtend it. The lowest of these bracts is the outer glume, which seals the opening to the cupule so that the kernel is obscured from view and protected from pests and granivores. At maturity, the rachid and the outer glume become extremely hardened (indurated), giving the cupulate fruitcase the appearance of a polished pebble. In maize, the rachid and glume are present but do not form a casing around the kernel, which is instead exposed on the ear for easy harvest.

Fig. 1. Ear of pure teosinte composed of eight cupulate fruitcases (left) and an ear of teosinte homozygous for the maize allele at *tga1* (right). The rachids (R) of teosinte are fully developed, forming a deep invagination in which the kernels are housed. The glume (G) seals the opening of the invagination so that the kernel is completely hidden and protected. The rachids of teosinte with the maize allele at *tga1* are less developed, forming only a short, shallow invagination that does not fully encase the kernel. The scale bar to the right is in millimeters.

We (*10*) identified a quantitative trait locus (QTL) on chromosome 4 controlling 42 to 50% of the phenotypic variance for outer glume induration and hypothesized that this locus represented a single gene with a dramatic phenotypic effect. This QTL appears to correspond to a factor affecting glume induration on chromosome 4 previously identified by other investigators (*11*). To investigate this QTL further, we transferred the segment of maize (Race Reventador, NAY-15) chromosome 4 containing this QTL into teosinte (*Z. mays* ssp. *parviglumis* Iltis and Cochrane 1981) by three generations of backcrossing coupled with positive selection for molecular-marker loci [restriction fragment length polymorphisms (RFLPs)] in the region flanking the QTL (Fig. 2). We also exercised negative selection on the maize alleles at RFLP loci outside the target region, enabling us to recover the teosinte (recurrent parent) genome rapidly. Similarly, we transferred the segment of teosinte (*Z. mays* ssp. *mexicana* Wilkes 48703) chromosome 4 containing this QTL into maize inbred line W22 by six generations of backcrossing. After the sixth backcross generation, a true-breeding line (W22-TGA) was recovered that possessed the W22 plant morphology except for the teosinte-like glumes in its ears.

To investigate this QTL, a segregating F_2 population was derived from the crossing of W22-TGA with the recurrent parent (W22). Of 230 F_2 progeny, 212 were scored for both glume induration and nine RFLP loci. The remaining 18 were scored only for

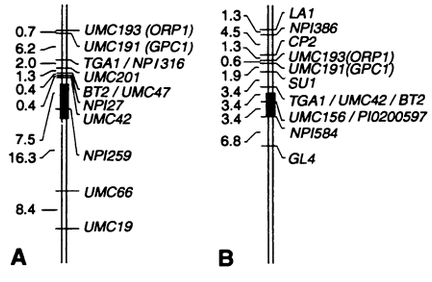

Fig. 2. Linkage maps of a portion of chromosome 4 showing the position of *tga1* and the marker loci used to localize it. Results from (**A**) the W22 × W22-TGA F_2 population and (**B**) the *la1-su1-gl4* (Maize Genetics Stock Center) × W22-TGA population. Black rectangles indicate the region in which the centromere is located.

J. Dorweiler, A. Stec, J. Doebley, Department of Plant Biology, University of Minnesota, St. Paul, MN 55108. J. Kermicle, Laboratory of Genetics, University of Wisconsin, Madison, WI 53706.

*To whom correspondence should be addressed.